

## A SUBARU SEARCH FOR Ly $\alpha$ BLOBS IN AND AROUND THE PROTOCLUSTER REGION AT REDSHIFT $z = 3.1^1$

YUICHI MATSUDA,<sup>2,3</sup> TORU YAMADA,<sup>2</sup> TOMOKI HAYASHINO,<sup>3</sup> HAJIME TAMURA,<sup>3</sup> RYOSUKE YAMAUCHI,<sup>3</sup> MASARU AJIKI,<sup>4</sup> SHINOBU S. FUJITA,<sup>4</sup> TAKASHI MURAYAMA,<sup>4</sup> TOHRU NAGAO,<sup>4</sup> KOUJI OHTA,<sup>5</sup> SADANORI OKAMURA,<sup>6,7</sup> MASAMI OUCHI,<sup>6</sup> KAZUHIRO SHIMASAKU,<sup>6,7</sup> YASUHIRO SHIOYA,<sup>4</sup> AND YOSHIAKI TANIGUCHI<sup>4</sup>

Received 2004 January 30; accepted 2004 April 15

### ABSTRACT

We report the properties of 35 robust candidate Ly $\alpha$  blobs (LABs), which are larger than 16 arcsec<sup>2</sup> in isophotal area and brighter than  $0.7 \times 10^{-16}$  ergs s<sup>-1</sup> cm<sup>-2</sup>, located in and around the protocluster region at redshift  $z = 3.1$  discovered by Steidel et al. in the SSA22 field, based on wide-field (31' × 23') and deep narrowband (NB497; 4977 Å, FWHM 77 Å) and broadband ( $B$ ,  $V$ , and  $R$ ) images taken with the prime-focus camera on the Subaru Telescope. The two previously known giant LABs are the most luminous and the largest in our survey volume of  $1.3 \times 10^5$  Mpc<sup>3</sup>. We reveal the internal structures of the two giant LABs and discover some bubble-like features, which suggest that intensive starburst and galactic superwind phenomena occurred in these objects in the past. The other 33 LABs have isophotal areas of  $\sim 16$ –78 arcsec<sup>2</sup> and flux of  $(0.7\text{--}7) \times 10^{-16}$  ergs s<sup>-1</sup> cm<sup>-2</sup>. These 35 LABs show a continuous distribution of isophotal area and emission-line flux. The distributions of average surface brightness and morphology are widespread from relatively compact high surface brightness objects to very diffuse low surface brightness ones. The physical origins of these LABs may be (1) photoionization by massive stars or active galactic nuclei, or (2) cooling radiation from gravitationally heated gas, or (3) shock heating by starburst-driven galactic superwind. One-third of the LABs are apparently not associated with ultraviolet continuum sources that are bright enough to produce Ly $\alpha$  emission, assuming a Salpeter initial mass function. Of these LABs 90% are located inside the high surface density region of the 283 relatively compact and strong Ly $\alpha$  emitters selected in our previous study. This suggests that these LABs may be phenomena related to a dense environment at high redshift.

**Key words:** cosmology: observations — galaxies: evolution — galaxies: formation — galaxies: high-redshift — galaxies: starburst

### 1. INTRODUCTION

Recently, Ly $\alpha$  imaging at high redshift revealed the existence of very luminous and extended Ly $\alpha$  nebulae, so-called Ly $\alpha$  blobs (LABs), which have a Ly $\alpha$  luminosity of more than  $10^{43}$  ergs s<sup>-1</sup> and a physical extent of about 100 kpc (e.g., Keel et al. 1999, hereafter K99; Steidel et al. 2000, hereafter S00; Francis et al. 2001, hereafter F01). These LABs are similar to the Ly $\alpha$  halos often seen around powerful radio galaxies at high redshift, but they are not associated with luminous radio sources (K99; S00; F01).

The ionization or excitation mechanisms of these LABs are unclear. Of these, two (No. 18 in K99 and 2142–4420 B1 in F01) are likely to have active galactic nuclei (AGNs), but two others (SSA22 blobs 1 and 2 in S00) show no evidence of

AGNs, although they are associated with Lyman break galaxies (LBGs) at the same redshift. It was shown, however, that none of these LABs have ultraviolet (UV) sources apparently bright enough to produce the extended photoionized Ly $\alpha$  emission line nebulae. Until now, three main ideas have been proposed to explain these LABs; (1) photoionization by UV sources obscured from our line of sight (e.g., Chapman et al. 2004), (2) cooling radiation from gravitationally heated gas in collapsed halos (S00; Haiman et al. 2000; Fardal et al. 2001), and (3) shock heating by starburst-driven galactic superwind (Taniguchi & Shioya 2000; Taniguchi et al. 2001; Ohyama et al. 2003). Scattering of Ly $\alpha$  photons by surrounding neutral gas may play an important role in all of these cases. Since all the LABs mentioned above are claimed to lie in protocluster regions, it is possible that the phenomena are related to a dense environment, in which early galaxy formation occurred preferentially (Governato et al. 1998) and which is possibly rich in hydrogen gas (e.g., Adelberger et al. 2003). Recently, Palunas et al. (2004) also reported their detection of a few candidate LABs associated with the overdensity region of Ly $\alpha$  emitters around 2142–4420 B1. On the other hand, there is more direct evidence that LABs are related to massive galaxy formation; luminous submillimeter sources were detected at SSA22 blobs 1, 2, and No. 18 (Chapman et al. 2001, 2004; Smail et al. 2003), while 2142–4420 B1 may not have been observed in submillimeter wavelengths. For another example, extended Ly $\alpha$  emission is also detected for a SCUBA source SMM 02399–0136 (Ivison et al. 1998; Vernet & Cimatti 2001).

<sup>1</sup> Based on data collected at the Subaru Telescope and in part obtained from the data archive at the Astronomical Data Analysis Center, which are operated by the National Astronomical Observatory of Japan.

<sup>2</sup> National Astronomical Observatory of Japan, Mitaka, Tokyo 181-8588, Japan; matsuda@awa.tohoku.ac.jp.

<sup>3</sup> Research Center for Neutrino Science, Graduate School of Science, Tohoku University, Aramaki, Aoba, Sendai 980-8578, Japan.

<sup>4</sup> Astronomical Institute, Graduate School of Science, Tohoku University, Aramaki, Aoba, Sendai 980-8578, Japan.

<sup>5</sup> Department of Astronomy, Kyoto University, Sakyo-ku, Kyoto 606-8502, Japan.

<sup>6</sup> Department of Astronomy, School of Science, University of Tokyo, Tokyo 113-0033, Japan.

<sup>7</sup> Research Center for the Early Universe, School of Science, University of Tokyo, Tokyo 113-0033, Japan.

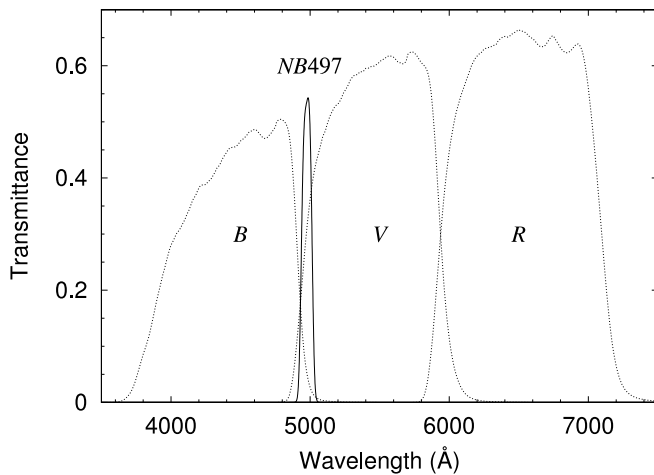


FIG. 1.—Transmittance of the NB497 (solid line),  $B$ -,  $V$ -, and  $R$ -band (dashed lines) filters for  $f/1.86$  beam of Suprime-Cam. The profiles include the CCD quantum efficiency of Suprime-Cam, the transmittance of the prime focus corrector, and the reflectivity of the primary mirror of Subaru Telescope.

The whole nature of LABs at high redshift is still far from understood. How typical are these 100 kpc scale LABs? What are the luminosity, size, and surface brightness distributions? How are they related to relatively compact Ly $\alpha$  emitters (LAEs), or LBGs, or AGNs? It is clear that we need to investigate a larger and systematic sample of LABs in order to understand their nature and relationship with galaxy formation.

Here we report the properties of 35 robust candidate LABs at  $z = 3.1$  in and around the protocluster region in the SSA22 field (S00), including SSA22 blobs 1 and 2, based on wide-field and very deep narrowband and broadband images taken with the 8.2 m Subaru Telescope. The properties of the relatively compact LAEs in the same field were presented in our previous paper (Hayashino et al. 2004, hereafter H04). While H04 also briefly mentioned the extended Ly $\alpha$  halos around LBGs in the field as well as the sky distribution of faint and low surface brightness “mini blobs” (MBs), here we present the results of a more objective detection and analysis of these LABs in order to discuss their nature in detail. We use AB magnitudes and adopt the following cosmological parameters in this paper:  $\Omega_M = 0.3$ ,  $\Omega_\Lambda = 0.7$ , and  $H_0 = 70 \text{ km s}^{-1} \text{ Mpc}^{-1}$ . In this cosmology, the universe at  $z = 3.1$  is 2.0 Gyr old, or 15% of the present age, and  $1''$  corresponds to 7.6 kpc of physical length at this redshift.

## 2. OBSERVATIONS

We obtained wide-field and deep narrowband (NB497) and broadband ( $B$ ,  $V$ , and  $R$ ) images centered at  $\alpha = 22^{\text{h}}17^{\text{m}}6^{\text{s}}$ ,  $\delta = +00^\circ 17'$  (J2000.0) on 2002 September 8 and 9 (UT) with the 8.2 m Subaru Telescope equipped with the prime-focus camera, Suprime-Cam (Miyazaki et al. 2002). The camera has 10 MIT/LL  $2048 \times 4096$  CCDs arranged in  $5 \times 2$  pattern, with the pixel scale of  $0''.20$  and a field of view of  $34' \times 27'$ . Our custom narrowband filter, NB497, has a central wavelength (CW) of  $4977 \text{ \AA}$  and a FWHM of  $77 \text{ \AA}$  to detect Ly $\alpha$  emission lines at  $z = 3.06\text{--}3.13$ . The spatial variations of the CW and FWHM of the NB497 filter are less than  $18$  ( $\Delta z = 0.015$ ) and  $5 \text{ \AA}$  ( $\Delta z = 0.004$ ), respectively. The profiles of the filters are shown in Figure 1. Total exposure times for each filter are listed in Table 1. Typical individual exposure times were 20 minutes for the narrow band and 6 minutes for the broad

TABLE 1  
SUMMARY OF OBSERVATIONS

Filter	Central Wavelength (Å)	Exposure (hr)	$1 \sigma$ (lim) (mag arcsec $^{-2}$ )
NB497 .....	4977	7.2	28.8
$B$ .....	4390	1.2	29.0
$V$ .....	5420	1.8	29.0
$R$ .....	6460	2.9	29.2
$BV$ .....	4977	...	29.1
$\text{NB}_{\text{corr}}$ .....	4977	...	28.8

bands with dither motions of more than  $30''$  between successive exposures. For the  $R$ -band, an additional 1.3 hr exposure of the same field taken from archive (2000 August and 2001 October, PI: E. M. Hu) was co-added.

The raw data are the same as presented in H04 and were reduced with IRAF and a custom software developed for Suprime-Cam data reduction (Yagi et al. 2002; Ouchi et al. 2003) in a manner similar to that presented in H04. We used the median sky image for flat-fielding and the mesh size parameter (as in the procedure of Yagi et al.) of  $30''$  for background sky subtraction before combining the images. The final images are slightly different from those used in H04, since we reduced the data by adopting a relatively large background mesh size to avoid the suppression of extended diffuse emission. All the stacked images were calibrated using spectrophotometric standard stars (Massey et al. 1988; Oke 1990) and Landolt standard stars (Landolt 1992). The magnitudes were corrected for Galactic extinction of  $E(B - V) = 0.08$ , as adopted by S00.

The combined images were aligned and smoothed with Gaussian kernels to match their seeing sizes. The average stellar profile of the final images has a FWHM of  $1''.0$ . We constructed a  $BV$  image [ $BV \approx (2B + V)/3$ ] for the continuum at the same effective wavelength as the narrowband filter and an emission-line  $\text{NB}_{\text{corr}}$  image by subtracting the  $BV$  image from the NB497 image. The limiting magnitudes ( $1 \sigma$ ) per square arcsecond are 28.8 (NB497), 29.0 ( $B_{\text{AB}}$ ), 29.0 ( $V_{\text{AB}}$ ), 29.2 ( $R_{\text{AB}}$ ), 29.1 ( $BV$ ), and 28.8 ( $\text{NB}_{\text{corr}}$ ). To evaluate these limiting magnitudes, we fitted a Gaussian function to the distributions of the sky counts that were obtained with apertures of  $1''.1$  diameter at random positions in each image and obtained the  $1 \sigma$  fluctuation values. We used only negative parts of the distributions in order to avoid contamination by objects, except for the  $\text{NB}_{\text{corr}}$  image.

The total size of the field analyzed here is  $31''.1 \times 22''.9$ . We masked out the edge region and the halos of the bright stars. The resultant total effective volume probed at  $z = 3.1$  by the narrowband imaging is  $1.3 \times 10^5 \text{ Mpc}^3$ .

## 3. SELECTION OF Ly $\alpha$ BLOBS

We obtained a sample of robust candidate LABs as follows. Object detection and photometry were performed using SExtractor version 2.2.2 (Bertin & Arnouts 1996). The object detection was made on the  $\text{NB}_{\text{corr}}$  image smoothed with a Gaussian kernel with a FWHM of  $1''$  and we adopted the criterion, 20 contiguous pixels above the threshold of  $6.3 \text{ counts pixel}^{-1}$ , which corresponds to  $28.0 \text{ mag arcsec}^{-2}$  ( $2.2 \times 10^{-18} \text{ ergs s}^{-1} \text{ cm}^{-2} \text{ arcsec}^{-2}$ ) or to the  $2 \sigma$  arcsec $^{-2}$  of the background fluctuation of the pre-smoothed  $\text{NB}_{\text{corr}}$  image. We adopted the deblending parameter of 0.05 and the

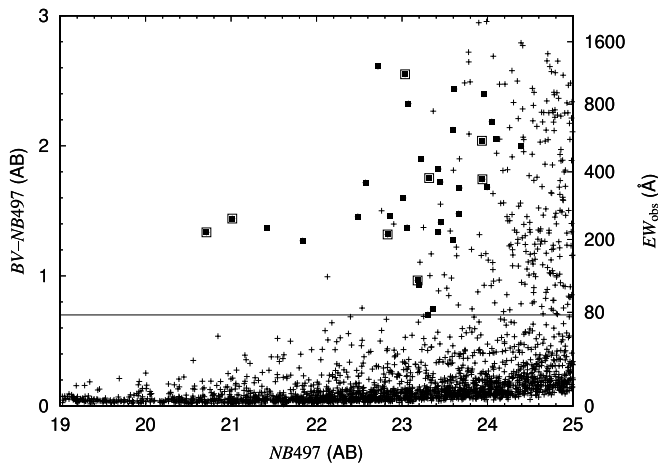


FIG. 2.—Color-magnitude diagram for  $BV - NB497$  color and  $NB497$  magnitude showing a color of  $BV - NB497 = 0.7$  (solid line), which corresponds to an observed equivalent width of  $80 \text{ \AA}$ . The filled squares show candidate LABs. The larger outlined squares show the candidates associated with known LBGs at  $z = 3.1$  in the SSA22a field (S03).

background mesh size of  $30'' \times 30''$ . The magnitudes and colors are measured for each object in the isophotal apertures defined in the process of source detection. In Figure 2, we plot the  $BV - NB497$  color versus  $NB497$  magnitude diagram for the  $NB_{\text{corr}}$ -selected sources with  $NB497 \leq 25$  mag. The solid line shows the limiting color for emission-line objects,  $BV - NB497 = 0.7$ , which corresponds to an observed equivalent width of  $80 \text{ \AA}$ . In Figure 3, we plot the isophotal area and the  $NB_{\text{corr}}$  magnitude of the emission line objects with  $BV - NB497 \geq 0.7$ . We selected 35 objects with the isophotal area larger than  $16 \text{ arcsec}^2$  (solid line), which corresponds to a spatial extent of  $30 \text{ kpc}$  at  $z = 3.1$ , as the robust candidate LABs in this paper. We note that the threshold is well above the values for point sources (dashed line). These 35 candidate LABs are indicated by the filled squares in Figures 2 and 3.

We checked the reliability of these 35 LABs on the  $NB_{\text{corr}}$  image in three different ways. First, we evaluated their significance above the background noise level on the  $NB_{\text{corr}}$  image assuming that the noise variation does not change significantly with the shape of photometric aperture. We measured  $1\sigma$  fluctuation of the sky counts in circular apertures with different diameters of  $1''$ – $20''$ . We found that all these LABs are significant at more than the  $8\sigma$  level (Fig. 3, dotted line). Second, we carried out the same detection and selection procedures on the reversed images constructed by multiplying the original images by  $-1$ . We did not find any false objects using this procedure. Finally, we divided the individual frames into two groups and stacked each to construct two independent images with half exposure time. We then measured their flux with the same apertures we defined on the total-exposure image. The flux measured on either of the two half-exposure frames is consistent with that of the total frame, within photometric errors, which supports the view that the features are not dominated by spurious objects in some peculiar frames.

We cannot completely rule out the possibility that our sample is contaminated by [O II]  $\lambda 3727$  at  $z = 0.33$ . However, the survey volume for [O II] lines is 22 times smaller than Ly $\alpha$ , and there are few known [O II] emitters with equivalent widths larger than  $60 \text{ \AA}$  (e.g., Hogg et al. 1998; Jansen et al. 2000).

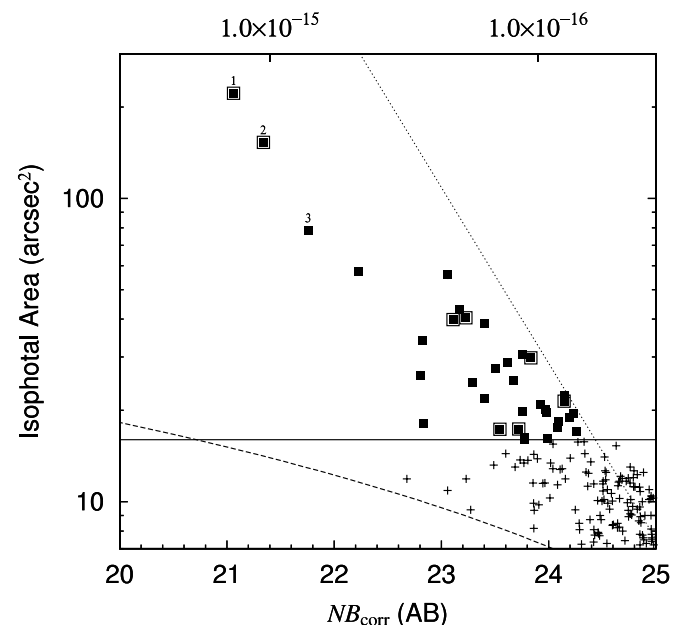


FIG. 3.—Distribution of isophotal area and magnitude on the  $NB_{\text{corr}}$  image for candidates of emission-line objects brighter than  $NB497 = 25.0$ . We selected objects with an isoarea larger than  $16 \text{ arcsec}^2$  (solid line) as candidate LABs (filled squares). The dashed line shows the expected value for point sources. The dotted line shows the  $8\sigma$  noise level of  $NB_{\text{corr}}$  magnitude for a given area. The large outlined squares show the candidates that are associated with known LBGs at  $z = 3.1$  in the SSA22a field (S03).

#### 4. RESULTS

In Table 2, we summarize the properties of the 35 confident candidate LABs; we denote them as LAB1 through LAB35 in order of isophotal area. Fourteen of these 35 objects are located in the SSA22a field studied in S00. Of the 14 sources, LAB1 and LAB2 are the same objects as the blob 1 and 2 in S00, and eight LABs are associated with the known LBGs at  $z = 3.1$  (Steidel et al. 2003, hereafter S03). These eight LABs are also indicated by the larger outlined squares in Figures 2, 3, 5, 6, 7, 9, and 10. As presented in H04, we detected 283 relatively compact LAEs in almost the same field (see H04 for more details). The 283 LAEs were selected with the criteria (1)  $NB497 < 25.8$ , (2)  $BV - NB497 > 1.2$ , (3-a)  $B_{\text{AB}} - V_{c,\text{AB}} > 0.2$  for objects with  $V_{c,\text{AB}} < 26.9$ , and (3-b)  $BV - NB497 > 1.5$  for objects with  $V_{c,\text{AB}} > 26.9$  using  $2''$  aperture photometry. Here  $V_{c,\text{AB}}$  represents the emission-line free  $V$ -band magnitude. Of these 35 LABs, 17 LABs with bright knots of emission lines were included in the LAE sample.

These 35 LABs seem to have a continuous distribution of the isophotal area and emission-line flux in Figure 3. LAB1 and LAB2 are the two most luminous and the largest emitters in our sample; they have isophotal area of  $222$  and  $152 \text{ arcsec}^2$ , respectively, and total emission-line flux brighter than  $1 \times 10^{-15} \text{ ergs s}^{-1} \text{ cm}^{-2}$ . We discovered another notably large emitter, LAB3, which has an area of  $78 \text{ arcsec}^2$  and flux of  $7 \times 10^{-16} \text{ ergs s}^{-1} \text{ cm}^{-2}$ , both about a factor of  $\sim 2$ – $3$  smaller than LAB1 and LAB2, while the average surface brightness is a little brighter. The remaining 32 LABs have isophotal areas of  $16$ – $57 \text{ arcsec}^2$  and flux values of  $0.7$ – $4.6 \times 10^{-16} \text{ ergs s}^{-1} \text{ cm}^{-2}$ .

The morphology and surface brightness profiles of these 35 LABs show a large variety, and some of them have interesting and complex structures. Figure 4 shows the  $U_n$ ,  $NB497$ ,  $NB_{\text{corr}}$ ,  $BV$ , and  $R$ -band images of these LABs. The  $U_n$ -band

TABLE 2  
PROPERTIES OF THE 35 CANDIDATE LABS

ID	R.A. <sup>a</sup> (arcmin)	Decl. <sup>a</sup> (arcmin)	NB <sub>corr</sub> (mag)	F(Ly $\alpha$ ) ergs s <sup>-1</sup> cm <sup>-2</sup> <sup>b</sup>	L(Ly $\alpha$ ) ergs s <sup>-1</sup> <sup>c</sup>	Area <sup>d</sup> (arcsec <sup>2</sup> )	$\langle SB \rangle$ (mag arcsec <sup>-1</sup> ) <sup>e</sup>	Notes S03	Notes H04 <sup>f</sup>
LAB1.....	18.0	7.9	21.06	1.3(−15)	1.1(+44)	222	26.9	SSA22a-C11 (blob 1)	
LAB2.....	14.8	8.7	21.34	1.0(−15)	8.5(+43)	152	26.8	SSA22a-M14 (blob 2)	
LAB3.....	9.8	10.7	21.76	7.0(−16)	5.8(+43)	78	26.5		LAE
LAB4.....	18.2	17.3	22.22	4.6(−16)	3.8(+43)	57	26.6		
LAB5.....	21.6	11.9	23.06	2.1(−16)	1.7(+43)	55	27.4		LAE
LAB6.....	26.6	20.1	23.17	1.9(−16)	1.6(+43)	42	27.3		LAE
LAB7.....	14.3	6.7	23.23	1.8(−16)	1.5(+43)	40	27.2	SSA22a-C6,M4	
LAB8.....	18.0	8.1	23.11	2.0(−16)	1.7(+43)	39	27.1	SSA22a-C15	
LAB9.....	11.8	12.6	23.40	1.5(−16)	1.3(+43)	38	27.4		LAE
LAB10.....	9.0	21.0	22.83	2.6(−16)	2.2(+43)	34	26.7		LAE
LAB11.....	19.4	12.7	23.76	1.1(−16)	9.1(+42)	30	27.5	(SSA22a-C47) <sup>g</sup>	
LAB12.....	16.6	12.2	23.83	1.0(−16)	8.6(+42)	29	27.5	SSA22a-M28	
LAB13.....	7.6	12.0	23.61	1.3(−16)	1.0(+43)	28	27.3		
LAB14.....	15.6	11.2	23.50	1.4(−16)	1.2(+43)	27	27.1		LAE
LAB15.....	7.5	5.6	22.81	2.7(−16)	2.2(+43)	26	26.4		2 LAEs
LAB16.....	18.3	6.5	23.67	1.2(−16)	9.9(+42)	25	27.2		LAE
LAB17.....	0.6	2.6	23.29	1.7(−16)	1.4(+43)	24	26.8		LAE
LAB18.....	17.3	3.1	24.14	7.8(−17)	6.4(+42)	22	27.5		
LAB19.....	19.6	13.9	23.40	1.5(−16)	1.3(+43)	21	26.8		LAE
LAB20.....	15.7	8.0	24.14	7.8(−17)	6.4(+42)	21	27.5	SSA22a-C12	
LAB21.....	5.3	7.4	23.92	9.5(−17)	7.9(+42)	20	27.2		
LAB22.....	15.8	18.7	23.97	9.1(−17)	7.6(+42)	20	27.2		
LAB23.....	7.6	18.4	23.75	1.1(−16)	9.2(+42)	19	27.0		LAE
LAB24.....	9.4	9.9	23.98	9.0(−17)	7.5(+42)	19	27.2		LAE
LAB25.....	18.9	11.0	24.23	7.2(−17)	5.9(+42)	19	27.5		
LAB26.....	12.0	12.7	24.20	7.4(−17)	6.1(+42)	18	27.4		
LAB27.....	22.7	16.6	24.10	8.1(−17)	6.7(+42)	18	27.3		
LAB28.....	9.8	18.0	22.83	2.6(−16)	2.2(+43)	18	26.0		LAE
LAB29.....	26.0	18.1	24.08	8.2(−17)	6.8(+42)	17	27.2		
LAB30.....	16.4	6.8	23.72	1.1(−16)	9.5(+42)	17	26.8	SSA22a-D3	
LAB31.....	14.8	6.3	23.55	1.3(−16)	1.1(+43)	17	26.6	SSA22a-C16	LAE
LAB32.....	18.5	17.1	24.26	7.0(−17)	5.8(+42)	17	27.3		LAE
LAB33.....	6.5	9.8	23.78	1.1(−16)	9.0(+42)	16	26.8		
LAB34.....	24.9	19.6	23.99	9.0(−17)	7.4(+42)	16	27.0		LAE
LAB35.....	18.3	12.5	23.78	1.1(−16)	9.0(+42)	16	26.8		LAE

<sup>a</sup> Using the coordinate system shown in Fig. 9.

<sup>b</sup> Ly $\alpha$  emission line flux.

<sup>c</sup> Ly $\alpha$  luminosity at  $z = 3.1$ .

<sup>d</sup> Isophotal area determined on the NB<sub>corr</sub> image.

<sup>e</sup> Average surface brightness on the NB<sub>corr</sub> image.

<sup>f</sup> (LAE) Ly $\alpha$  emitter.

<sup>g</sup> No redshift information in S03.

images of the SSA22a and 22b fields (the SSA22a field is shown in Fig. 9, *dashed line*, and the SSA22b field is centered 9' south of that position) are taken from the ftp site listed in S03.<sup>8</sup> We show just isophotal areas for the objects outside the SSA22a and 22b fields. Each panel is 25'' on a side. We adopted the same intensity scaling for all panels so that their surface brightness in any passband is compared directly. The yellow lines show the isophotal apertures of the emission-line nebulae. The cyan crosses in the *R*-band images show the Ly $\alpha$  peak positions. The green and magenta lines in the *R*-band images show the isophotal apertures of the associated LBGs at  $z = 3.1$  and the nearest continuum sources to the Ly $\alpha$  peak, respectively, with a threshold of 28.0 mag arcsec<sup>-2</sup>. LAB1 and LAB2 appear to have several “bubble-like” structures, which we examine in more detail in Figure 8. LAB5 and LAB6 show elongated, somewhat conical structures. LAB8 (SSA22a-C15)

is located at 15'' north of LAB1 and is likely a part of it. LAB9 and LAB26 are also located close to each other with a separation of  $\sim 10''$ ; there is another compact LAE between them. LAB27 is very clumpy and shows the four knots of emission lines within 15'' separation. LAB18, 20, 25, 26, and 32 appear very diffuse.

Note that, while our continuum subtraction works sufficiently well, there still remain patches of over or under subtraction at the positions of the bright continuum sources in the NB<sub>corr</sub> images in Figure 4 (i.e., LAB4, LAB10, LAB13, LAB30, and LAB33). We examined the effects of these patches in determining the isophotal apertures of these LABs and confirmed that the apertures are well determined, avoiding these patches. LAB20 have an over subtracted patch at the position of the LBG, but this can also be caused by Ly $\alpha$  absorption in the galaxy. Loss of line flux by these patches is as small as a few percent of the total in any case. In addition to the effects of continuum subtraction, we also note that LAB7 (SSA22a-C6 and M14) lies close to the halo of a bright star

<sup>8</sup> See [ftp://ftp.astro.caltech.edu/pub/ccs/lbgsurvey](http://ftp.astro.caltech.edu/pub/ccs/lbgsurvey).

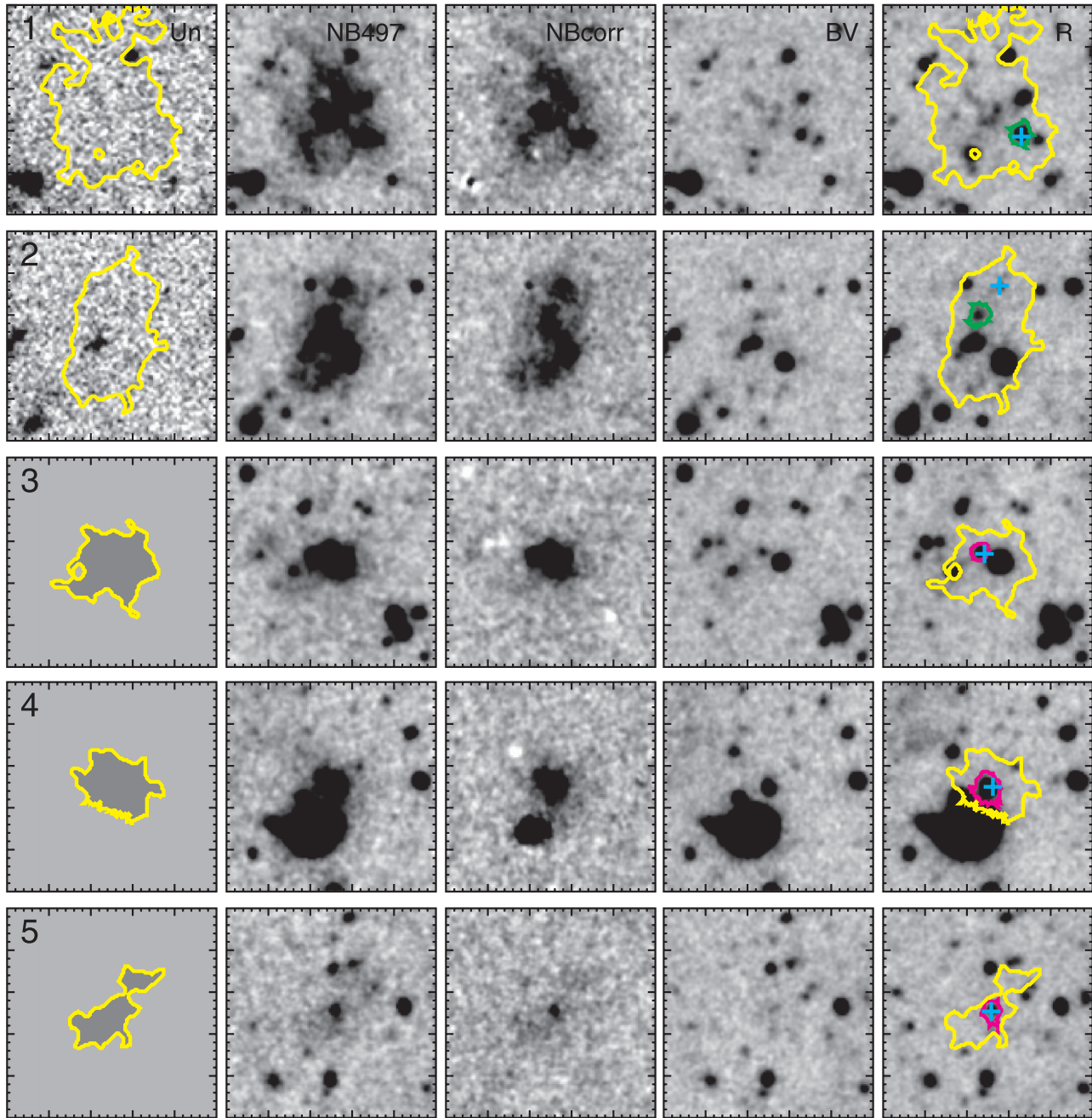


FIG. 4.— $U_n$  (or just isophotal areas), NB497, NB<sub>corr</sub>, BV, and R images of the 35 candidates LABs. Each panel is 25'' square with the candidate centered. The yellow lines show the isophotal apertures. The R-band images show the Ly $\alpha$  peak positions (cyan crosses), the associated LBGs at  $z = 3.1$  (green lines), and the nearest continuum sources to the Ly $\alpha$  peaks (magenta lines).

and LAB17 is located near the edge of the image where noise level is relatively high.

In Figure 5, we plot the isophotal area versus the average surface brightness on the NB<sub>corr</sub> image of the 35 LABs. The solid and dashed lines are the same as those in Figure 3, but the dotted line shows the average surface brightness, 27.6 mag arcsec $^{-2}$ , which is the resulting practical detection limit. Although the original detection threshold for 20 pixels (0.8 arcsec $^2$ ) is 28.0 mag arcsec $^{-2}$ , in practice the extended objects with average surface brightness as low as this limit are easily divided into some smaller pieces by noise in the detection procedure. As can be seen in Figure 5, the distribution of the average surface brightness is widespread from

relatively compact high surface brightness objects to very diffuse low surface brightness objects. However, there is no source with an average surface brightness between 27.0 and 27.6 mag arcsec $^{-2}$  and an isophotal area larger than 60 arcsec $^2$ . If there are sources in this “void” of LABs, they should be detected with  $S/N > 8$  as shown in Figure 3. It is worth confirming that there is no such largely extended LAB with lower surface brightness than LAB1 and LAB2, in order to recognize the rarity of such gigantic LABs. We checked this by a simple test; the isophotal areas of LAB1 and LAB2 are still larger than 100 arcsec $^2$ , applying a 0.7 mag brighter threshold in our source detection. This suggests that if there are LABs with lower surface brightness but with surface

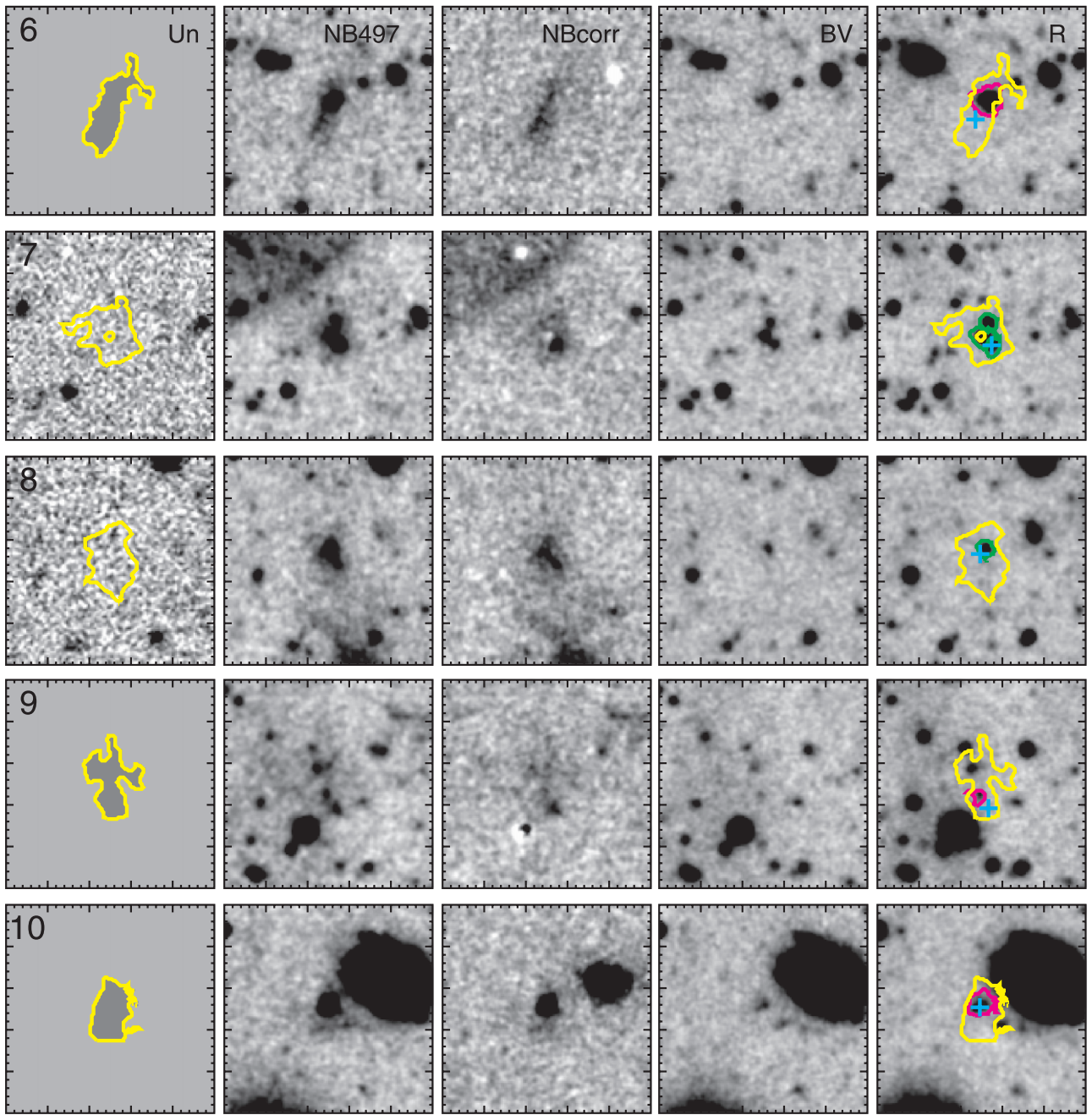


FIG. 4.—Continued

brightness profiles similar to LAB1 and LAB2, we can detect them as objects with large isophotal area. We also examined how the mesh size in our sky subtraction affects the detection of large and diffuse objects. With our adopted mesh size of  $900 \text{ arcsec}^2$ , flux from the objects up to about  $450 \text{ arcsec}^2$  is not significantly ( $<50\%$ ) affected by the procedure, even for a case of constant surface brightness. In this sense, we also confirmed that LAB1 is the largest Ly $\alpha$  object in this field.

In Figure 6, we plot the isophotal area versus the  $R$  magnitudes of the continuum sources to see the relation between the spatial extents of Ly $\alpha$  nebulae and continuum flux. If we select all the continuum sources inside the isophotal area, the  $R$  magnitudes must be overestimated. We detected about

43,000 objects down to  $R = 25.5$  mag in our field of view of  $31' \times 23'$ . The surface density of the objects is  $0.017 \text{ arcsec}^{-2}$ . The possibility that an unrelated object is inside the halo of  $4'' \times 4''$  by chance is as large as 0.3 for each LAB. Therefore, we selected the continuum sources located nearest to the peak of the Ly $\alpha$  emission in the  $R$ -band image (i.e., the sources inside the magenta lines in Fig. 4) as the candidate counterparts. For the eight objects that are associated with the known LBGs at  $z = 3.1$ , we selected the LBGs as the associated continuum sources (i.e., the sources inside the green lines in Fig. 4). The distribution of the  $R$  magnitudes of these associates is widespread, especially for smaller LABs, and we cannot find any correlation in Figure 6.

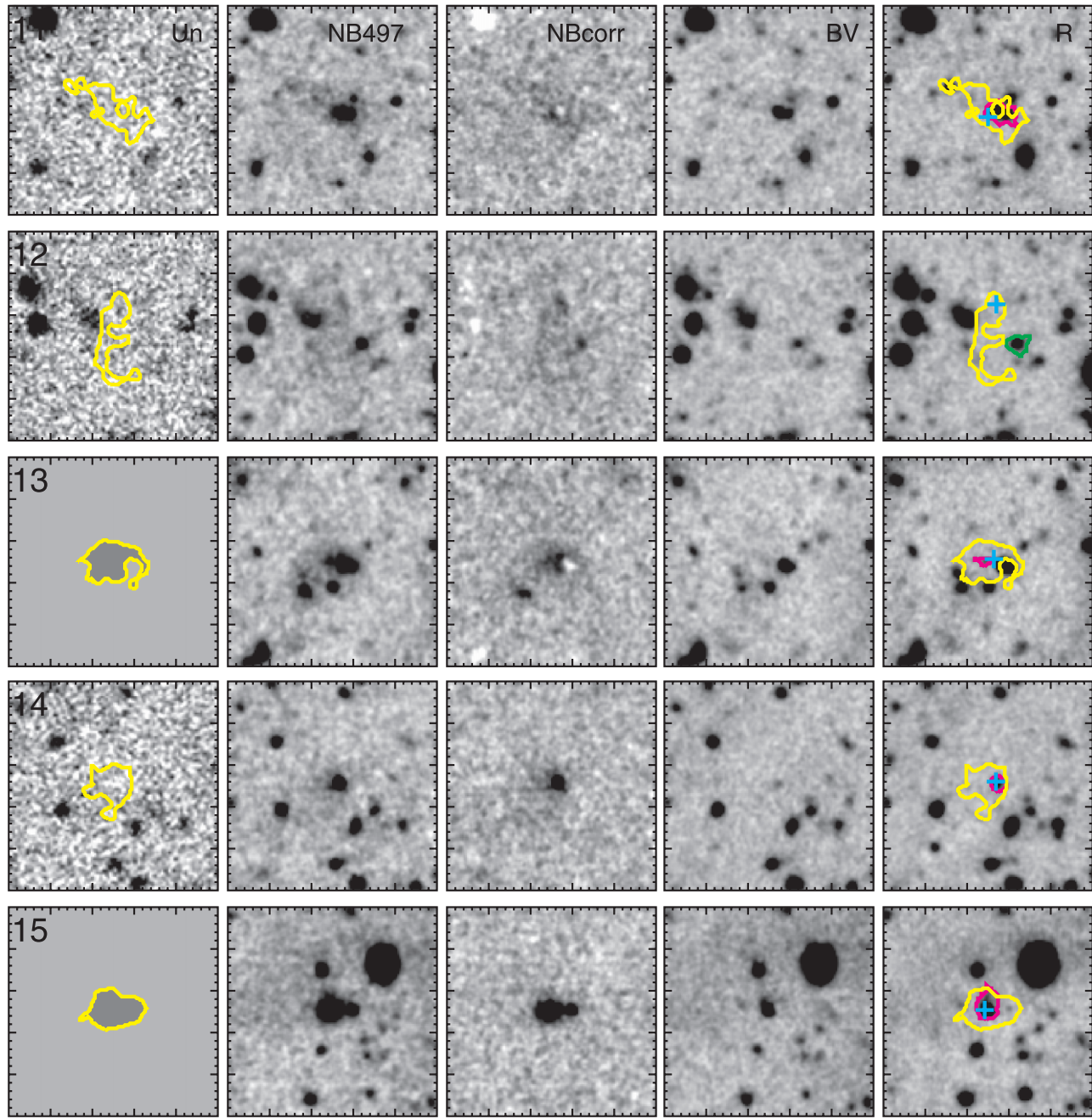


FIG. 4.—Continued

In Figure 7, we plot the isophotal area versus the difference of position angles (P.A.'s) of emission-line nebulae and continuum sources. We used the same continuum sources as in Figure 6. The isophotal axes of the continuum sources and the emission-line nebulae tend to align with the radio sources for powerful radio galaxies at high redshift (the “alignment effect,” e.g., McCarthy et al. 1987). In this case, the differences of P.A. are around 0. If we see bipolar flows from galaxy disks, the differences may be around 90. However, there seems to be no correlation in Figure 7.

In Figure 8, we show the NB497 and the NB<sub>corr</sub> images of the three most luminous and largest objects in our sample with contour levels of emission-line surface brightness to see their

internal structures. The contour lines are at 3, 6, and 9  $\sigma$  of the sky-background fluctuation per square arcsecond (27.6, 26.8, and 26.1 mag arcsec $^{-2}$ ). Very complicated structures are seen in LAB1 and LAB2, while rather smooth halo-like structure is seen in LAB3. The position of the CO emission line and submillimeter continuum source in LAB1 is  $\Delta\text{R.A.} = 13''$ ,  $\Delta\text{decl.} = 13''$  in Figure 8 (Chapman et al. 2004). We clearly confirmed the cavity of Ly $\alpha$  emission at the position of the CO source (Bower et al. 2004). We can recognize “bubble-” or “shell-like” round-shaped structures in the NB497 or NB<sub>corr</sub> images of LAB1 and LAB2 (blobs 1 and 2 in S00); the centers and radii ( $r$ ) of these bubbles are ( $\Delta\text{R.A.}, \Delta\text{decl.}, r$ ) (7 $''$ 2, 17 $''$ 2, 3 $''$ 0), (12 $''$ 4, 7 $''$ 5, 2 $''$ 2), (11 $''$ 6, 14 $''$ 3, 1 $''$ 4), and (15 $''$ 1, 11 $''$ 1, 1 $''$ 4) for

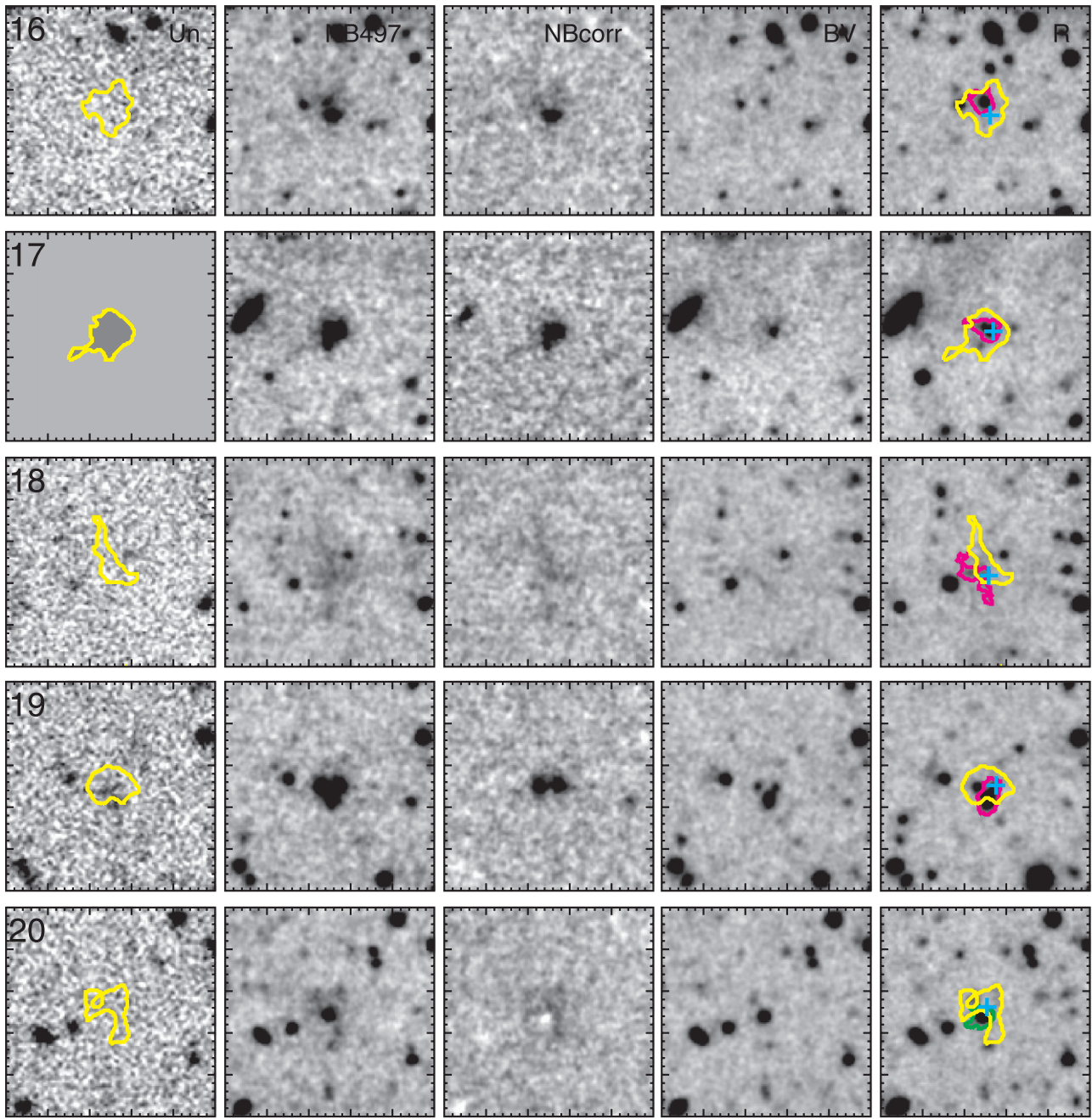


FIG. 4.—Continued

LAB1 and (10<sup>''</sup>5, 8<sup>''</sup>2, 2<sup>''</sup>5) and (15<sup>''</sup>0, 15<sup>''</sup>1, 1<sup>''</sup>8) for LAB2 in Figure 8. We discuss possible origins of these complicated structures in the next section.

In Figure 9, we plot the sky distribution of the 35 LABs (Fig. 9, top) and the 283 relatively compact LAEs from H04 (Fig. 9, bottom). The solid lines in both figures show the high-density region (HDR) in which the local surface number density of the LAEs is larger than the mean value of the entire field. The dashed line shows the field of view of S00 (the SSA22a field). The overall sky distribution of the 35 LABs is very similar to the HDR of the LAEs, which implies that these LABs belong to the same structure as the LAEs. Note that the difference of the limiting magnitudes inside and outside the HDR is only 0.02.

We also checked whether or not these candidates are associated with known radio sources, since such Ly $\alpha$  emission line nebulae are often seen around high-redshift radio galaxies. None of them is associated with a radio source brighter than the total flux of 1 mJy at 1.4 GHz (FIRST catalog; White et al. 1997). This 1 mJy FIRST detection limit corresponds to  $2 \times 10^{32}$  ergs s<sup>-1</sup> Hz<sup>-1</sup> at a rest frequency of 6 GHz for objects at  $z = 3.1$ , which is about 2 orders of magnitude fainter than powerful radio galaxies. We also checked the association of X-ray sources and did not find any counterparts in the ROSAT All-Sky Survey (RASS) source catalog (Voges et al. 1999, 2000). The typical limiting flux in the 0.1–2.4 keV band of the RASS is  $\sim 10^{-13}$  ergs cm<sup>-2</sup> s<sup>-1</sup>, which corresponds to  $\sim 10^{46}$  ergs s<sup>-1</sup> for objects at  $z = 3.1$ . This limit is

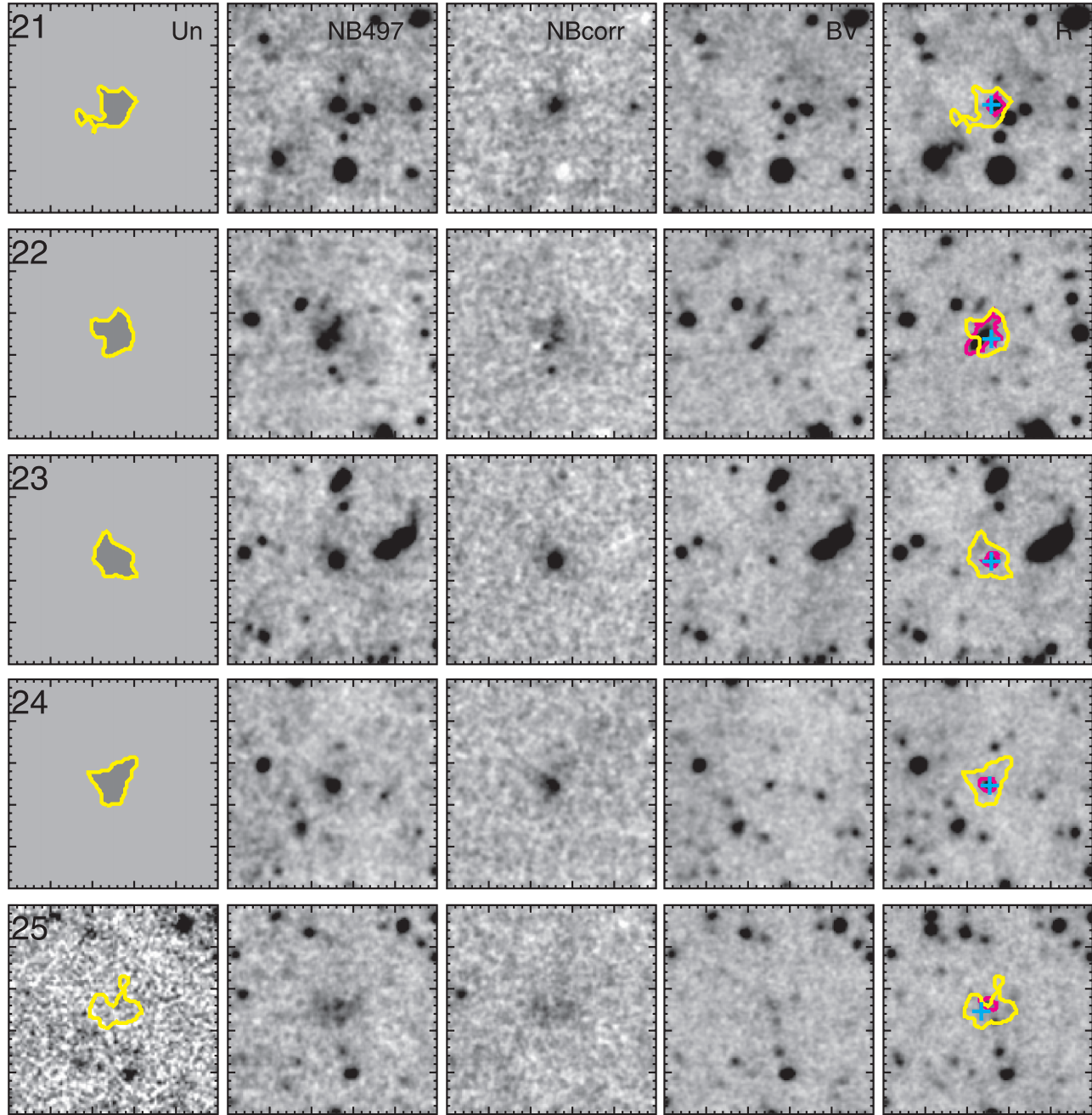


FIG. 4.—Continued

comparable to the luminosity of the brightest AGNs in X-ray. Deeper X-ray images by *Chandra* or *XMM-Newton* will help us investigate the presence or absence of AGNs in these LABs.

## 5. DISCUSSION

We first argue that most of the 35 candidates must be LABs at  $z = 3.1$ . This is supported by the large equivalent widths, larger sampled volume than [O II] emitters at  $z = 0.33$ , association with LBGs (60% in the SSA22a field), and the coincidence of overall spatial distribution with that of LAEs selected by more robust equivalent width criteria (H04).

In § 5.1., we discuss the properties of the 35 LABs and consider what their physical origins are and how they are related to the galaxy formation process.

### 5.1. Ly $\alpha$ Blobs and Galaxy Formation Process

As discussed in § 1, there are at least three possibilities for the origin of these LABs, namely (1) photoionization, (2) cooling radiation from gravitationally heated gas in collapsed halos, and (3) shock heating by starburst-driven galactic superwind. Scattering by surrounding neutral gas affects their appearance for all these cases. The cases of cooling radiation and superwind represent rather early and late stages of intensive star formation in protogalaxies, while photoionization by internal sources

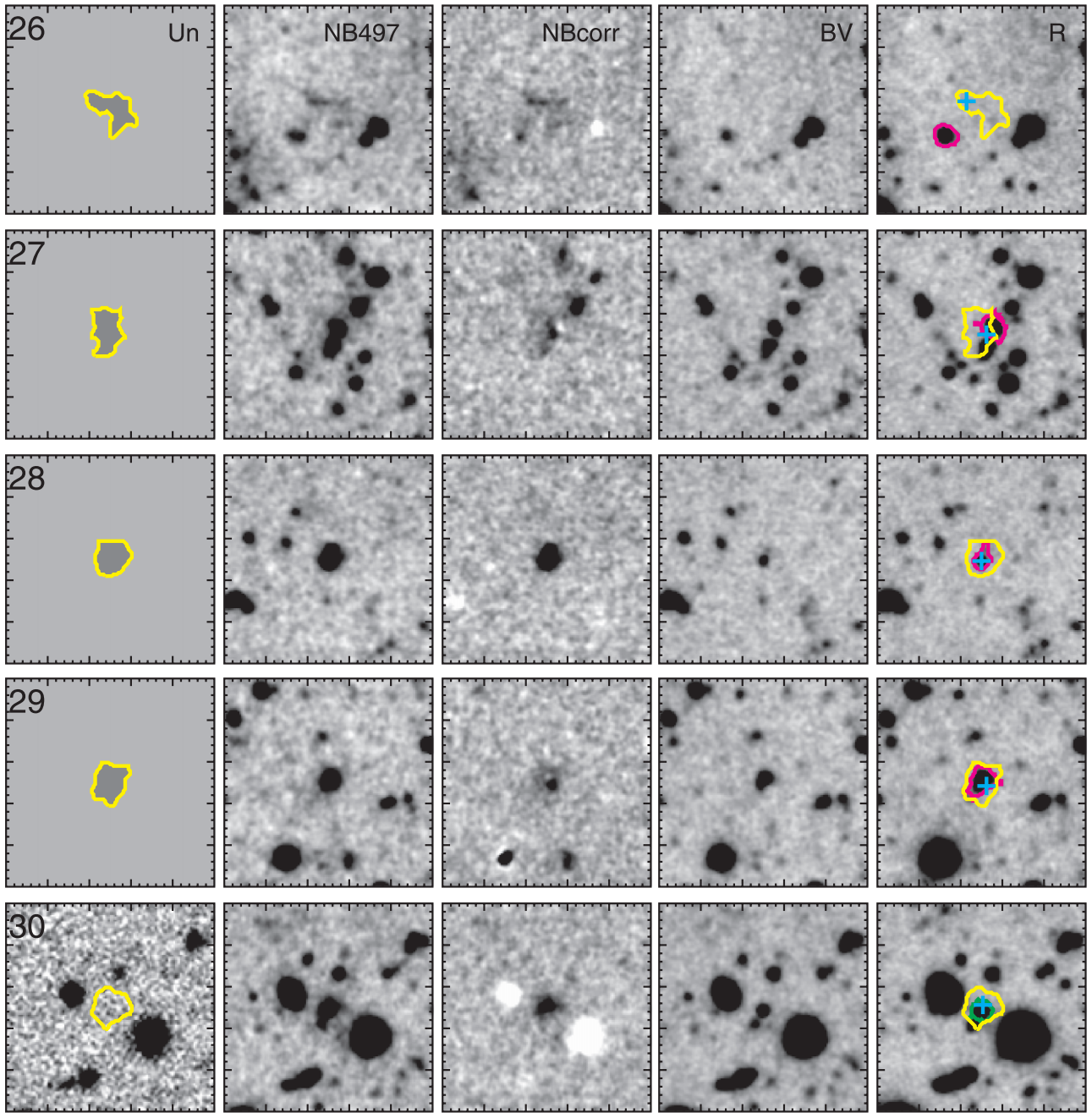


FIG. 4.—Continued

represents on-going events. Sources of photoionization may be massive stars or AGNs inside the galaxies, or the background diffuse UV emission. It is interesting to see the objects in the same large-scale structure and possibly at different phases of galaxy formation.

#### 5.1.1. Photoionization

Probably, the simplest idea is that we see extended star-forming regions in protogalaxies or diffuse hydrogen gas surrounding or bound to the protogalaxies, which is ionized by photons that escaped from galactic star-forming regions. Note that emission-line nebulae in our sample seem to be more extended than the continuum sources (see Fig. 4) and some of them indeed resemble extended diffuse gas structures of pro-

to galaxies at high redshift studied in numerical simulation (e.g., Abadi et al. 2003).

In order to test this picture, namely, photoionization by galactic star-forming regions, we compare the Ly $\alpha$  luminosities with the UV luminosities of the associated objects to see for how many sources the observed UV luminosities are apparently sufficient to produce the Ly $\alpha$  emission by photoionization.

In Figure 10, we plot  $R$  versus  $NB_{corr}$  diagram for these 35 LABs. The filled squares with  $1\sigma$  error bars show magnitudes calculated by the same isophotal apertures as used in § 3 (Fig. 10, left). We translated the  $NB_{corr}$  and  $R$  magnitude into the equivalent star formation rates (SFR) at  $z = 3.1$ , assuming the same Salpeter initial mass function (IMF; Salpeter 1955)

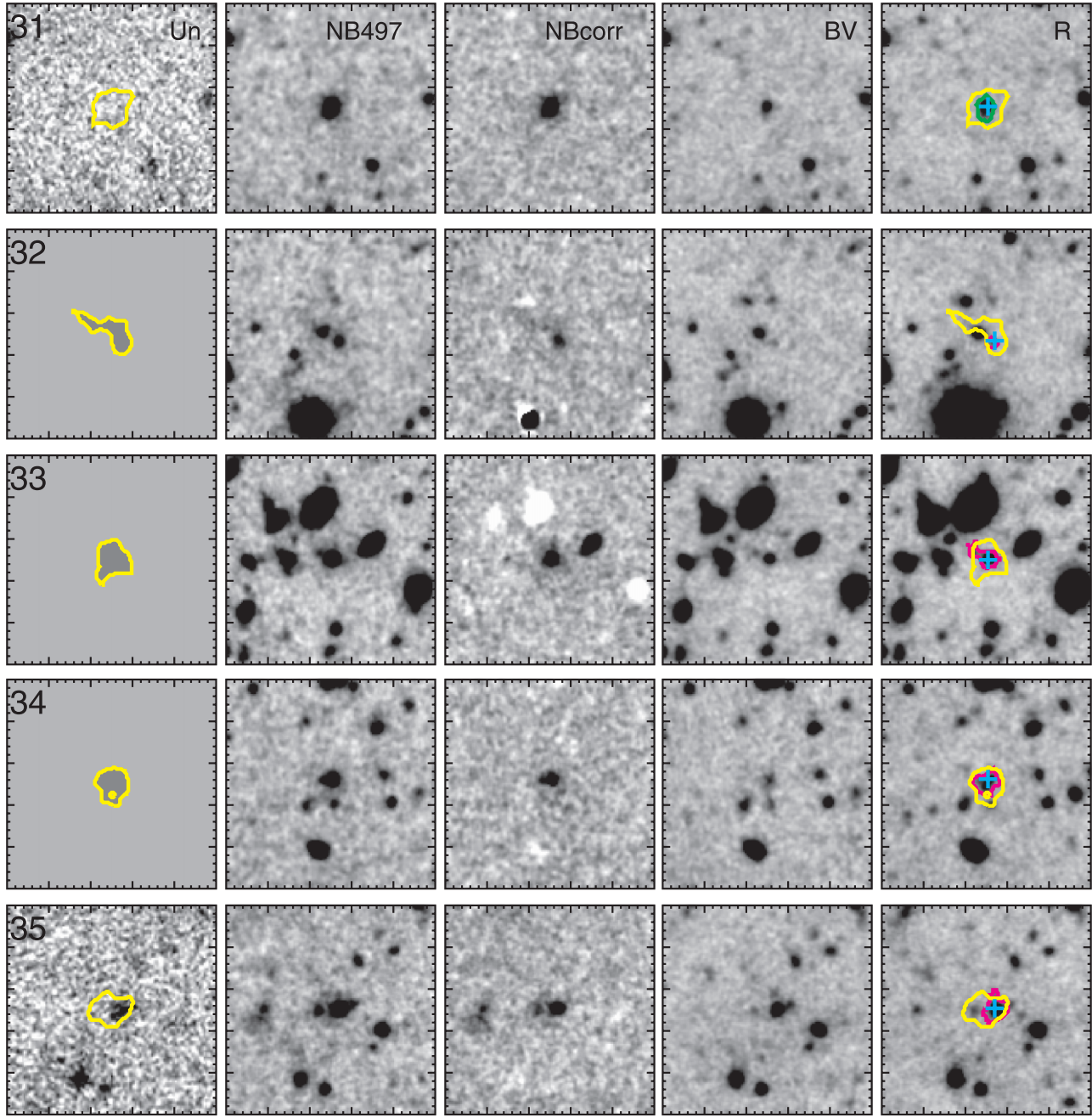


FIG. 4.—Continued

with mass limits 0.1 and  $100 M_{\odot}$ , solar metallicity, no extinction, and case B recombination in the low-density limit ( $N_e \ll 1.5 \times 10^4 \text{ cm}^{-3}$ ). We used the relationships,  $L(\text{Ly}\alpha) = 1.0 \times 10^{42} (\text{SFR}/M_{\odot} \text{ yr}^{-1})$  ergs  $\text{s}^{-1}$  for Ly $\alpha$  luminosity (Osterbrock 1989; Kennicutt 1998) and  $L_{\nu}(\text{UV}) = 7 \times 10^{27} (\text{SFR}/M_{\odot} \text{ yr}^{-1})$  ergs  $\text{s}^{-1} \text{ Hz}^{-1}$  for UV luminosity (Kennicutt 1998). Of course, the large isophotal apertures suffer from contamination by the foreground and background continuum sources in the  $R$ -band image and the contribution of UV luminosity in Figure 10 (*left*) must be overestimated as mentioned in § 4. Therefore, to evaluate a more reasonable contribution from the UV continuum sources, we also plotted the same diagram in Figure 10 (*right*), but selecting the same continuum sources as in Figure 6, namely, associated LBGs or the nearest sources to the Ly $\alpha$

peak. In the right and left panels, respectively, of Figure 10, 6 and 14 of the 35 LABs have  $\text{SFR}(\text{Ly}\alpha) > \text{SFR}(\text{UV})$  and thus are apparently not associated with stellar UV continuum sources that are bright enough to produce photoionized Ly $\alpha$  emission. Thus, for about one-third of the 35 LABs, simple photoionization by massive stars is not sufficient to explain the Ly $\alpha$  luminosities. Note that we neglect the dilution effect of UV continuum flux for this comparison. This means we consider a simple limiting case in which the LAB completely surrounds the continuum source and is optically thick in the Lyman continuum, thereby absorbing all the available ionizing photons.

We may consider at least four possibilities to explain these Ly $\alpha$ -excess objects that have  $\text{SFR}(\text{Ly}\alpha) > \text{SFR}(\text{UV})$  as

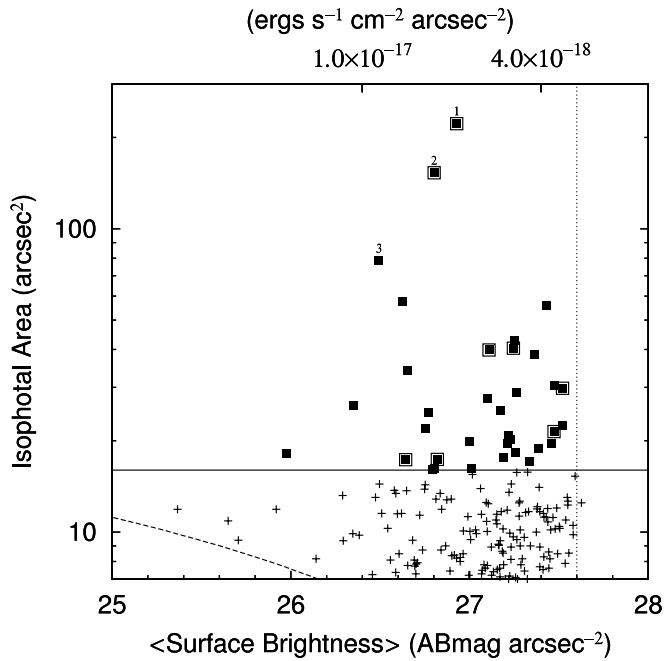


FIG. 5.—Distribution of isophotal area and average surface brightness on the NB<sub>corr</sub> image for the 35 candidate LABs (filled squares). Lines show the sample threshold of the isophotal area for LABs (16 arcsec<sup>2</sup>; solid line), the resulting practical detection limit of average surface brightness  $\sim 27.6$  mag arcsec<sup>-2</sup> (dotted line), and the expected distribution for point sources (dashed line). The large outlined squares show the candidates that are associated with known LBGs at  $z = 3.1$  in the SSA22a field (S03).

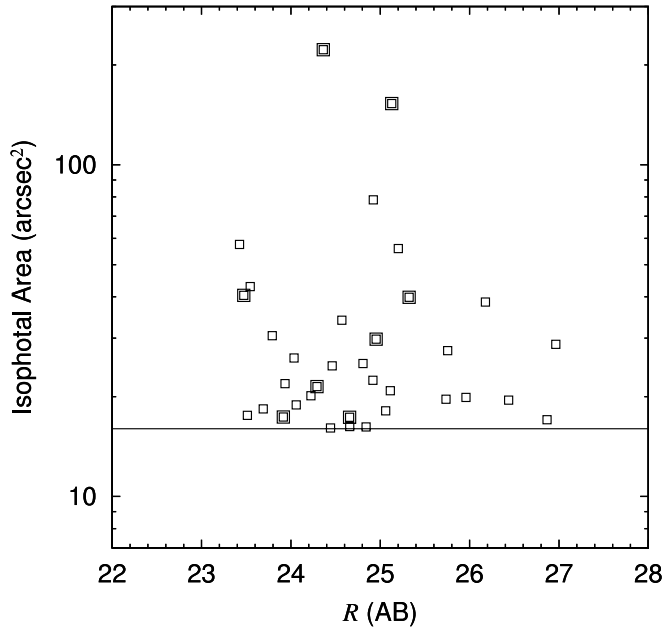


FIG. 6.—Distribution of isophotal area vs.  $R$  magnitudes of the continuum sources. We selected the continuum sources located nearest to the peak of the Ly $\alpha$  emission in the  $R$ -band image (i.e., the sources inside the magenta lines in Fig. 4). For the eight objects that are associated with known LBGs at  $z = 3.1$ , we selected the LBGs as the continuum sources (i.e., the sources inside the green lines in Fig. 4). The solid line shows the threshold of the isophotal area for LABs (16 arcsec<sup>2</sup>). The bold squares show the candidates that are associated with known LBGs at  $z = 3.1$  in the SSA22a field (S03).

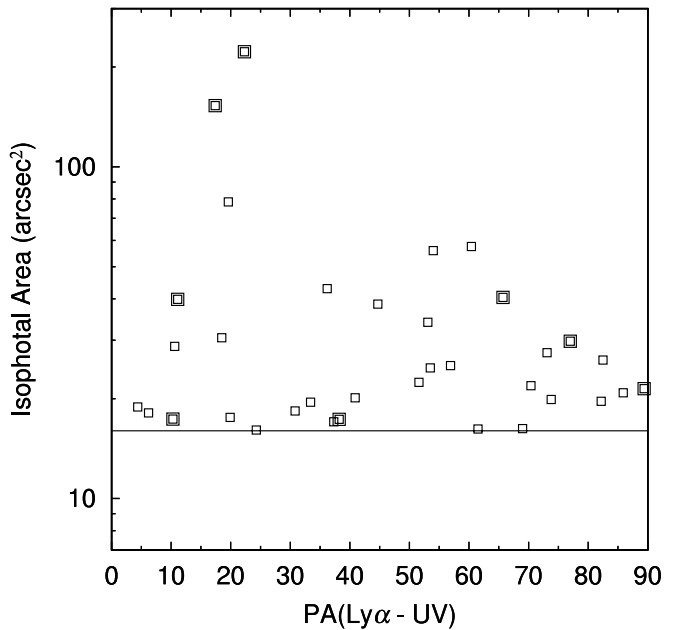


FIG. 7.—Distribution of isophotal area and difference of position angles of the emission line nebulae and the continuum sources. We used the same continuum sources as in Fig. 6. The solid line shows the threshold of the isophotal area for LABs (16 arcsec<sup>2</sup>). The bold squares show the candidates that are associated with known LBGs at  $z = 3.1$  in the SSA22a field (S03).

shown in the right panel of Figure 10. The first one is that the UV spectra of these objects are dominated by a stellar population with more massive, metal-poor, young stars. These Ly $\alpha$ -excess objects have rest Ly $\alpha$  equivalent widths  $EW_{rest}$  larger than 100 Å. In order to explain such large Ly $\alpha$  equivalent widths, we need to consider a more extreme stellar population. Charlot & Fall (1993) showed that a younger starburst age or a flatter IMF with a high-mass cutoff are needed to explain a large equivalent width,  $EW_{rest} \gtrsim 100$  Å. For example, the Large Area Ly $\alpha$  Survey found  $\approx 150$  LAEs at  $z = 4.5$ , and 60% of them have  $EW_{rest}$  larger than 240 Å (Malhotra & Rhoads 2002). They claimed that a stellar IMF with an extreme slope of  $\alpha = 0.5$  or zero-metallicity stars are required to produce such large Ly $\alpha$  equivalent widths.

The second possibility is that the gas is photoionized by AGNs inside forming galaxies (e.g., Haiman & Rees 2001). Of the 14 Ly $\alpha$ -excess sources, three (LAB23, LAB24, and LAB28) have pointlike nearest continuum sources that have a FWHM smaller than 1''.1 on the  $R$ -band image. The UV luminous object LAB21 also has a point continuum source. Comparison with a deep X-ray image or optical spectroscopy to detect strong C IV emission is needed to further constrain the association with AGNs. However, since the nearest continuum sources are not pointlike but resolved galaxies in many other cases, we do not think the AGN population dominates our sample.

The third possibility is that ionizing UV sources (AGNs or star formation) may be hidden from our line of sight. There are cases in which the peaks of Ly $\alpha$  emission are not coincident with the continuum sources (LAB9, LAB13, and LAB25 for Ly $\alpha$  excess objects, and LAB6, LAB16, LAB18, and LAB26 for UV luminous objects). Five of these seven continuum sources have redder  $V_C - R$  colors (0.3–0.4 mag) than those of other sources that are close to the peak of Ly $\alpha$  emission ( $r \lesssim 1''$ ). If this is due to misidentification of associated continuum sources, true continuum sources may be additional fainter objects. Indeed, it is known that submillimeter and

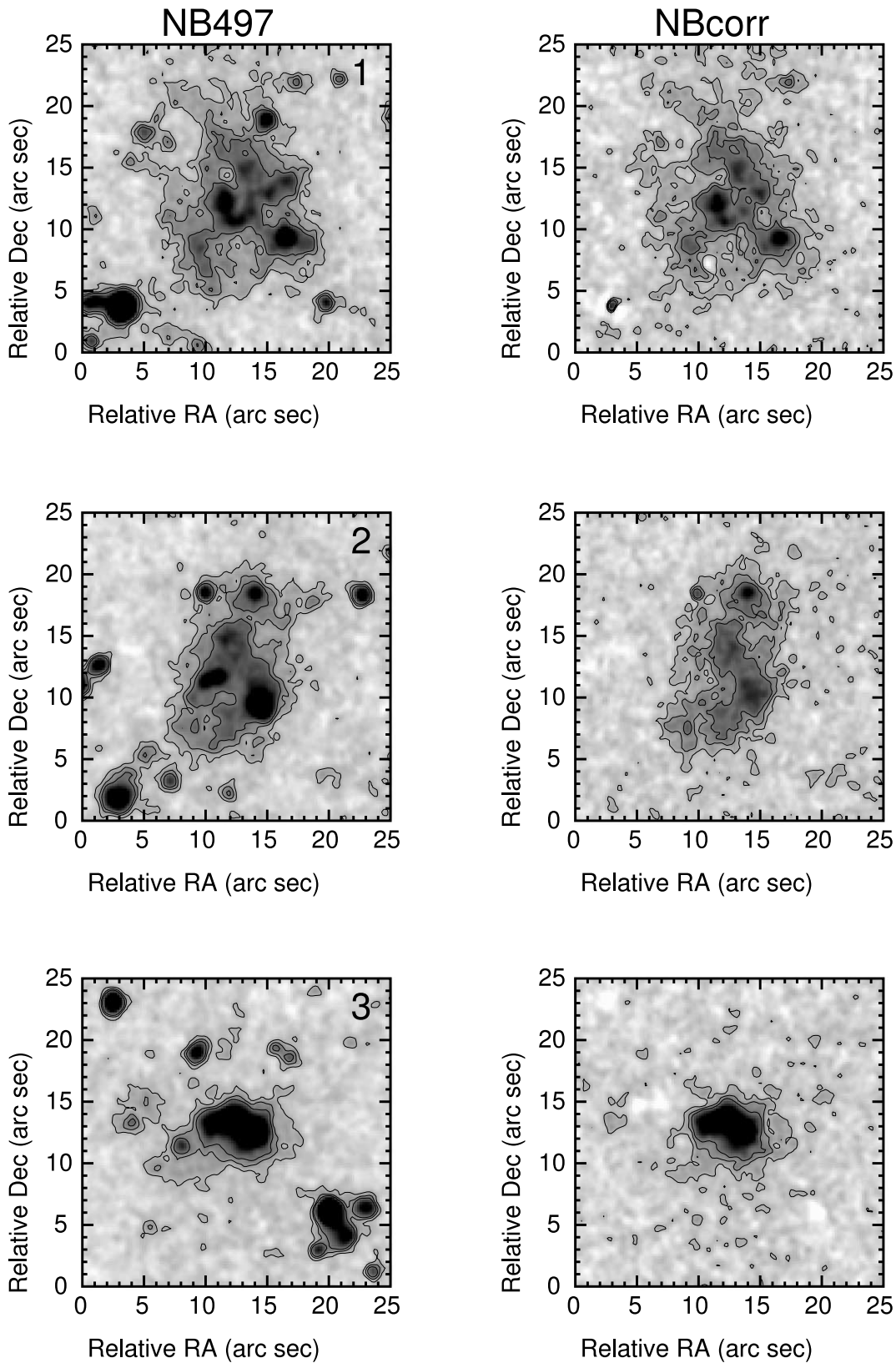


FIG. 8.—NB and  $\text{NB}_{\text{corr}}$  images of the three most luminous and largest LABs in our sample. The contour lines are at levels of  $3, 6,$  and  $9 \sigma \text{ arcsec}^{-2}$  ( $27.6, 26.8,$  and  $26.1 \text{ mag arcsec}^{-2}$ ).

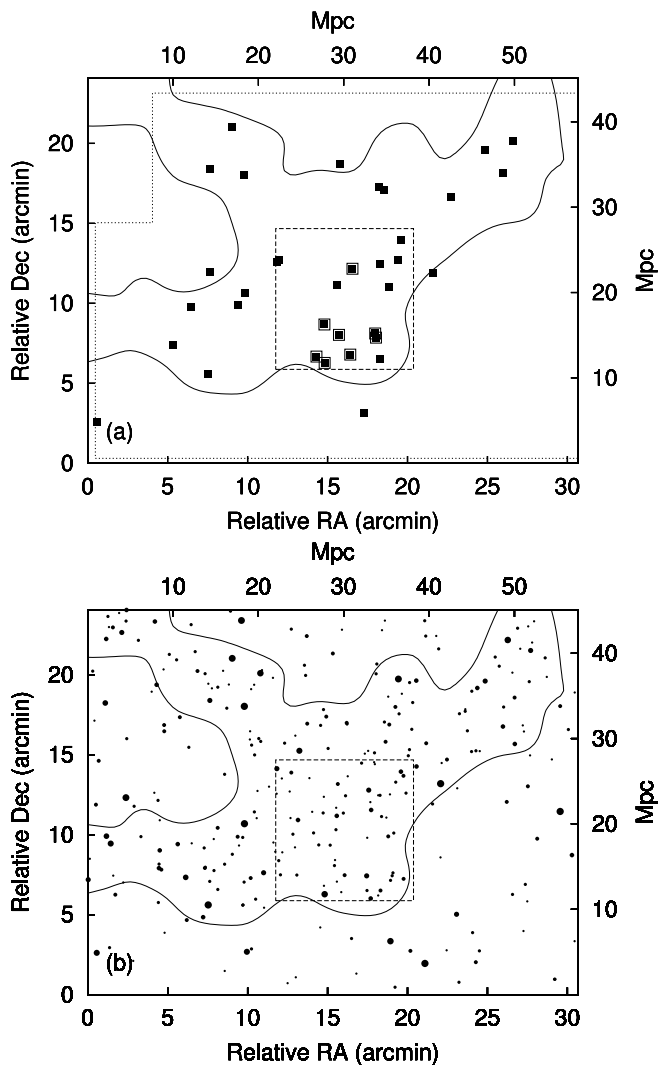


Fig. 9.—*Top:* Spatial distribution of the 35 candidate LABs. *Bottom:* Relatively compact 283 LAEs presented by Hayashino et al. (2004). The contours show the high-density region (HDR) of the 283 LAEs, the dotted line in the top panel shows the region used in this paper, the dashed line shows the SSA22a field, and the large outlined squares show the candidates that are associated with known LBGs at  $z = 3.1$  (S03).

CO emission is detected in LAB1 but apart from the position of the known LBG (Chapman et al. 2001, 2004). The amount of hidden star formation for these objects is expected to be from several to 100  $M_{\odot}$  yr $^{-1}$  as seen in Figure 10, assuming no extinction for Ly $\alpha$  emission.

The last possibility, especially for very diffuse LABs, is photoionization of hydrogen gas in the outer part of galaxies caused by diffuse intergalactic UV background. Some authors evaluated diffuse Ly $\alpha$  emission from systems ionized by background UV radiation. For example, Gould & Weinberg (1996) evaluated properties of Ly $\alpha$  emission from Ly $\alpha$  clouds with neutral hydrogen column density of  $10^{17}$ – $10^{20}$  cm $^{-2}$ . They found that the typical surface brightness of the Ly $\alpha$  clouds is  $10^{-19}$  ergs s $^{-1}$  cm $^{-2}$  arcsec $^{-2}$  at  $z = 3$ , and this value has a weak dependence on column density. Our detection limit,  $\sim 3 \times 10^{-18}$  ergs s $^{-1}$  cm $^{-2}$  arcsec $^{-2}$  is still considerably brighter than this value.

#### 5.1.2. Cooling Radiation from Gravitationally Heated Gas

Besides photoionization by massive stars or AGNs, we should take into account the contribution of cooling radiation

from gravitationally heated gas in collapsed halos (Rees & Ostriker 1977; S00; Haiman et al. 2000; Fardal et al. 2001). Since this is a direct consequence of the atomic gas cooling process during galaxy formation, it is very important to find objects radiating Ly $\alpha$  emission by this mechanism. Typical flux and size,  $\sim 10^{-17}$ – $10^{-16}$  ergs s $^{-1}$  cm $^{-2}$  and  $\sim 5''$ – $10''$  (e.g., Table 1 in Haiman et al. 2000) roughly match with the objects discussed in this paper.

According to the simulation by Fardal et al. (2001), objects with large radiative cooling with  $L(\text{Ly}\alpha_{\text{cool}}) > 10^{43}$  ergs s $^{-1}$  also have high star formation activity and the total Ly $\alpha$  luminosities of such objects become larger than  $10^{44}$  ergs s $^{-1}$ . Below these luminosities, however, cooling radiation sometimes dominates Ly $\alpha$  emission. Given the luminosity range of our sample of 35 LABs,  $6 \times 10^{42}$  to  $10^{44}$  ergs s $^{-1}$ , it is possible that objects dominated by cooling radiation are contained in our sample.

Interestingly, there are several objects that are very diffuse and are not associated with bright continuum sources (LAB5, LAB8, LAB9, LAB13, and LAB25). They are good candidates of the Ly $\alpha$  cooling objects. There are also objects with extended faint halo structure, although they are associated with relatively bright continuum sources (LAB6, LAB7, LAB11, LAB12, LAB18, and LAB26).

#### 5.1.3. Superwind

Next we discuss the case of shock heating by starburst-driven galactic superwind. Expanding bubbles are one example of direct evidence of superwind activities (e.g., Heckman et al. 1990). The bubble-like structures of LAB1 and LAB2 (blob 1 and 2) resemble the expanding bubble observed in Arp 220 with H $\alpha$  imaging (e.g., Heckman et al. 1996). Note that the possible bubbles (see § 4) have a typical radius of  $2''$ , corresponding to 15 kpc at  $z = 3.1$ , which is similar to the radius of the bubble in Arp 220. Interestingly, it is known that LAB1 is more luminous by a factor of 30 than Arp 220 and has a very similar rest-frame optical and far-infrared spectral energy distribution (Taniguchi et al. 2001). Ohyama et al. (2003) showed that a bright knot in the central part of LAB1 ( $\Delta R.A. = 11''$  and  $\Delta \text{Decl.} = 11''$ , Fig. 8) has three velocity components separated by approximately  $\pm 3000$  km s $^{-1}$  and two component profiles found both at  $1''$ – $2''$  northwest and  $1''.5$ – $2''.5$  southeast of the knot. These profiles may represent the expanding shocked shells. We considered star formation activities to produce each bubble assuming the same expanding timescale of  $3 \times 10^7$  yr and kinetic energy injection rate of  $\sim 10^{43}$  ergs s $^{-1}$  as those of Arp 220 (i.e., Heckman et al. 1996). We use the fraction of supernova energy converted to kinetic energy of 0.3 (e.g., Mori et al. 2002) and the number of supernovae per solar mass of stars formed of 0.007, assuming a Salpeter IMF (e.g., Bower et al. 2001). Then we have the supernovae rate of  $\sim 1$  yr $^{-1}$  and SFR  $\sim 150 M_{\odot}$  yr $^{-1}$  for each bubble. Since we have identified at least four bubbles in LAB1, it has total SFR of more than  $\sim 600 M_{\odot}$  yr $^{-1}$ . This is on the same order as the expected currently on-going SFR  $\geq 500 h^{-2} M_{\odot}$  yr $^{-1}$  of LAB1 from submillimeter observations (Chapman et al. 2001).

On the other hand, Bower et al. (2004) argued that the Ly $\alpha$  emission of LAB1 is driven by the interaction of outflowing material and the inflow of material cooling in the cluster potential from the chaotic velocity structure they observed. They suggested that the emission-line halo around NGC 1275 in the Perseus cluster may be a good local analog to LAB1, although LAB1 is a factor of  $\sim 100$  more luminous

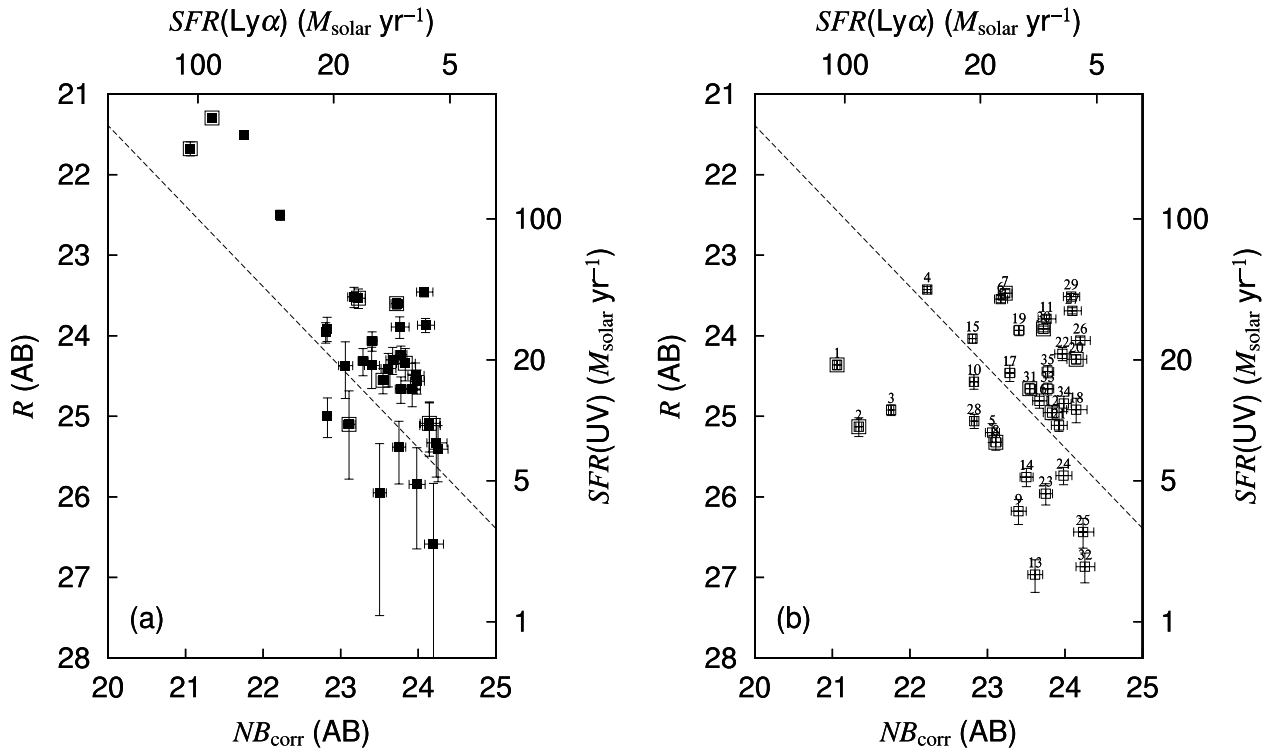


FIG. 10.—Distributions of  $R$  and  $NB_{\text{corr}}$  magnitudes for the 35 candidate LABs. Magnitudes in the left panel are measured on the same isophotal apertures determined with the  $NB_{\text{corr}}$  image. The  $R$  magnitudes in the right panel are those of continuum sources nearest to the Ly $\alpha$  peak or the known LBGs at  $z = 3.1$ . The dashed line shows  $SFR(\text{Ly}\alpha) = SFR(\text{UV})$ . The large outlined squares show the candidates that are associated with known LBGs at  $z = 3.1$  in the SSA22a field (S03).

and has a larger velocity width. They also argued, however, that the Ly $\alpha$  emission is unlikely to be explained by cooling flow phenomenon alone from the low  $L_X/L_{\text{Ly}\alpha}$  ratio. We note that a number of superbubbles occurred rather simultaneously, which may also explain the observed chaotic velocity structure.

Bower et al. (2004) also showed that two LBGs (SSA22a C11 and C15 in S00) have clear velocity shear patterns in their Ly $\alpha$  emission line (LAB1 and LAB8 here). They suggested that the shear patterns are bipolar outflows by superwind.

### 5.2. Sky Distribution of These LABs

An interesting result presented in this paper is that these LABs seem to be correlated with a dense environment of LAEs in H04. While 72% of the LAEs (205/283) are located in the HDR, 86% of these LABs (30/35) are in the HDR and the other 3 are just outside the HDR but may be in the same structure (see Fig. 9). Using a simulation we evaluated the probability that more than 30 of 35 sources randomly selected from the 283 LAE sample would be in the HDR and found a 5.7% probability. If we consider the case of 33/35 sources, it is only 0.1%. Thus, the distribution of the LABs is likely to be more concentrated in the HDR than that of the 283 LAEs. Furthermore, we note that one-third of these LABs are clustered at the SSA22a field where the two giant blobs (LAB1 and LAB2) exist.

What does the strong clustering of these LABs mean? The simplest idea may be, therefore, that these extended and probably gas-rich objects trace the region in which galaxy formation preferentially occurs at  $z \sim 3$ . Previous numerical simulations coupled with semianalytic galaxy-formation models claimed that the galaxy formation occurs in a biased manner at high redshift and concentrations of star-forming galaxies

observed at  $z \sim 3$  evolve into rich clusters at a later epoch (Governato et al. 1998; Kauffmann et al. 1999).

Since the distribution of more massive dark matter halos is more strongly biased to mass at high redshift in these models, it is also possible that the extended emitters trace more massive objects than LAEs. Unfortunately, our sample of LABs is not large enough to estimate mass from their spatial clustering properties. We may, however, use their spatial extents to constrain their mass in the case that the extended Ly $\alpha$  nebulae are bound to the galaxies. If we assume that the dark matter halos of the LABs were collapsed at  $z = 3.1$  and the extents of Ly $\alpha$  nebulae are smaller than the virial radii, we can evaluate the lower-limit of the mass. The virial mass of a dark matter halo collapsed at redshift  $z$  can be written as  $M = 4\pi R_{\text{vir}}^3 \rho_{\text{crit}}(z) \Delta_c(z)/3$ . Here  $R_{\text{vir}}$  is the virial radius,  $\rho_{\text{crit}}(z)$  is the critical density at that redshift, and  $\Delta_c(z)$  is the virial density. We use the fitting formula of Bryan & Norman (1998) for the virial density taken from the solution to the collapse of a spherical top-hat perturbation,  $\Delta_c = 18\pi^2 + 82x - 39x^2$ , where  $x \equiv \Omega_M(z) - 1$ . The average isophotal area of the 35 LABs is 37 arcsec $^2$ , which is equivalent to an area of a circle with a radius of 3'4 or 26 kpc in physical scale at  $z = 3.1$ . With this value, the lower limit of the mass is  $4 \times 10^{10} M_\odot$ . This limit is very similar to the lower limit of the average dynamical mass of LBGs at  $z \sim 2$  estimated from their rotation curves (Erb et al. 2003); although, it is rather small compared with a typical mass of LBGs of  $\sim 10^{12} M_\odot$  estimated from their clustering properties at  $z \sim 3$  (Adelberger et al. 1998).

Another possibility is that the clustering may be due to an environment that is relatively rich in neutral hydrogen. The density of intergalactic Ly $\alpha$  clouds may be high inside the large-scale structure of star-forming galaxies. Indeed, Adelberger et al. (2003) found that the transmission of Ly $\alpha$

forest at  $z = 3.1$  in the SSA22a field (i.e., Fig. 9, *dashed line*) is very low. In such an environment, the gas clouds bound to or around galaxies would tend to be observed as extended diffuse Ly $\alpha$  nebulae.

## 6. CONCLUSIONS AND FUTURE PROSPECTS

We present the first large and systematic sample of LABs at high redshift. The 35 LABs show a continuous distribution of the isophotal area and the emission-line flux and a variety of the morphology and surface brightness. At least three different origins (photoionization, cooling radiation, and superwind) are considered to explain their properties. In order to reveal their true nature, however, we need further deep spectroscopic observations to investigate their kinematic properties, ionization, and excitation status, and metallicity in the future. Deep and wide-field  $U$ -band imaging of the field will also be useful

in the determination of the true associated continuum sources. Further wide-field narrowband imaging in other fields will prove their clustering properties with higher statistical accuracy, especially their concentration relative to the more compact and stronger LAEs.

We thank the staff of the Subaru Telescope for their assistance with our observations. This work is partially supported by the grants-in-aid for scientific research of the Ministry of Education, Culture, Sports, Science, and Technology (14540234). The Image Reduction and Analysis Facility (IRAF) used in this paper is distributed by the National Optical Astronomy Observatory, which is operated by the Association of Universities for Research in Astronomy, Inc., under contact to the National Science Foundation.

## REFERENCES

- Abadi, M. G., Navarro, J. F., Steinmetz, M., & Eke, V. R. 2003, ApJ, 591, 499  
 Adelberger, K. L., Steidel, C. C., Giavalisco, M., Dickinson, M., Pettini, M., & Kellogg, M. 1998, ApJ, 505, 18  
 Adelberger, K. L., Steidel, C. C., Shapley, A. E., & Pettini, M. 2003, ApJ, 584, 45  
 Bertin, E., & Arnouts, S. 1996, A&AS, 117, 393  
 Bower, R. G., Benson, A. J., Lacey, C. G., Baugh, C. M., Cole, S., & Frenk, C. S. 2001, MNRAS, 325, 497  
 Bower, R. G., et al. 2004, MNRAS, in press (astro-ph/0402456)  
 Bryan, G. L., & Norman, M. L. 1998, ApJ, 495, 80  
 Chapman, S. C., Lewis, G. F., Scott, D., Richards, E., Borys, C., Steidel, C. C., Adelberger, K. L., & Shapley, A. E. 2001, ApJ, 548, L17  
 Chapman, S. C., Scott, D., Windhorst, R. A., Frayer, D. T., Borys, C., Lewis, G. F., & Ivison, R. J. 2004, ApJ, 606, 85  
 Charlot, S., & Fall, S. M. 1993, ApJ, 415, 580  
 Erb, D. K., Shapley, A. E., Steidel, C. C., Pettini, M., Adelberger, K. L., Hunt, M. P., Moorwood, A. F. M., & Cuby, J. 2003, ApJ, 591, 101  
 Fardal, M. A., Katz, N., Gardner, J. P., Hernquist, L., Weinberg, D. H., & Dav, R. 2001, ApJ, 562, 605  
 Francis, P. J., et al. 2001, ApJ, 554, 1001  
 Gould, A., & Weinberg, D. H. 1996, ApJ, 468, 462  
 Governato, F., Baugh, C. M., Frenk, C. S., Cole, S., Lacey, C. G., Quinn, T., & Stadel, J. 1998, Nature, 392, 359  
 Haiman, Z., & Rees, M. J. 2001, ApJ, 556, 87  
 Haiman, Z., Spaans, M., & Quataert, E. 2000, ApJ, 537, L5  
 Hayashino, T., et al. 2004, AJ, submitted  
 Heckman, T. M., Armus, L., & Miley, G. K. 1990, ApJS, 74, 833  
 Heckman, T. M., Timothy, M., Dahlem, M., Eales, S. A., Fabbiano, G., & Weaver, K. 1996, ApJ, 457, 616  
 Hogg, D. W., Cohen, J. G., Blandford, R., & Pahre, M. A. 1998, ApJ, 504, 622  
 Ivison, R. J., Smail, I., Le Borgne, J. F., Blain, A. W., Kneib, J. P., Bezeccourt, J., Kerr, T. H., & Davies, J. K. 1998, MNRAS, 298, 583  
 Jansen, R. A., Fabricant, D., Franx, M., & Caldwell, N. 2000, ApJS, 126, 271  
 Kauffmann, G., Colberg, J. M., Diaferio, A., & White, S. D. M. 1999, MNRAS, 307, 529  
 Keel, W. C., Cohen, S. H., Windhorst, R. A., & Waddington, I. 1999, AJ, 118, 2547  
 Kennicutt, R. C., Jr. 1998, ARA&A, 36, 189  
 Landolt, A. U. 1992, AJ, 104, 340  
 Malhotra, S., & Rhoads, J. E. 2002, ApJ, 565, L71  
 Massey, P., Strobel, K., Barnes, J. V., & Anderson, E. 1988, ApJ, 328, 315  
 McCarthy, P. J., van Breugel, W., Spinrad, H., & Djorgovski, S. 1987, ApJ, 321, 29  
 Miyazaki, S., et al. 2002, PASJ, 54, 833  
 Mori, M., Ferrara, A., & Madau, P. 2002, ApJ, 571, 40  
 Ohyama, Y., et al. 2003, ApJ, 591, L9  
 Oke, J. B. 1990, AJ, 99, 1621  
 Osterbrock, D. E. 1989, *Astrophysics of Gaseous Nebulae and Active Galactic Nuclei* (Mill Valley: University Science Books)  
 Ouchi, M., et al. 2003, ApJ, 582, 60  
 Palunas, P., Teplitz, H. I., Francis, P. J., Williger, G. M., & Woodgate, B. E. 2004, ApJ, 602, 545  
 Rees, M. J., & Ostriker, J. P. 1977, MNRAS, 179, 541  
 Salpeter, E. E. 1955, ApJ, 121, 161  
 Smail, I., Ivison, R. J., Gilbank, D. G., Dunlop, J. S., Keel, W. C., Motohara, K., & Stevens, J. A. 2003, ApJ, 583, 551  
 Steidel, C. C., Adelberger, K. L., Shapley, A. E., Pettini, M., Dickinson, M., & Giavalisco, M. 2000, ApJ, 532, 170  
 ———. 2003, ApJ, 592, 728  
 Taniguchi, Y., & Shioya, Y. 2000, ApJ, 532, L13  
 Taniguchi, Y., Shioya, Y., & Kakazu, Y. 2001, ApJ, 562, L15  
 Vernet, J., & Cimatti, A. 2001, A&A, 380, 409  
 Voges, W., Aschenbach, B., Boller, T., Bräuninger, H., Briel, U., & Burkert, W. 2000, IAU Circ., 6420, 1  
 Voges, W., et al. 1999, A&A, 349, 389  
 White, R. L., Becker, R. H., Helfand, D. J., & Gregg, M. D. 1997, ApJ, 475, 479  
 Yagi, M., Kashikawa, N., Sekiguchi, M., Doi, M., Yasuda, N., Shimasaku, K., & Okamura, S. 2002, AJ, 123, 66